Dynamical regimes of vortex flow in type-II superconductors with parallel twin boundaries

Harshwardhan Chaturvedi,[1] Nathan Galliher,[1] Ulrich Dobramysl,[2] Michel Pleimling,[1,3] and Uwe C Täuber[1]

[1] *Department of Physics & Center for Soft Matter and Biological Physics, Virginia Tech, Blacksburg, Virginia 24061-0435, United States*
[2] *Wellcome Trust / CRUK Gurdon Institute, University of Cambridge, Tennis Court Rd, Cambridge CB2 1QN, United Kingdom*
[3] *Academy of Integrated Science, Virginia Tech, Blacksburg, Virginia 24061-0405, United States*

(Dated: October 11, 2017)

We explore the dynamics of driven magnetic flux lines in disordered type-II superconductors in the presence of twin boundaries oriented parallel to the direction of the applied magnetic field, using a three-dimensional elastic line model simulated with Langevin molecular dynamics. The lines are driven perpendicular to the planes to model the effect of an electric current applied parallel to the planes and perpendicular to the magnetic field. A study of the long-time non-equilibrium steady states for several sample thicknesses L and drive strengths F_d reveals a rich collection of dynamical regimes spanning a remarkably broad depinning transition region that separates the pinned and moving-lattice states of vortex matter. We perform novel direct measurements of flux line excitations such as half-loops and double kinks, and quantitatively analyze their excitation occurrence distributions to characterize the topologically rich flux flow profile and generate a boundary curve separating the regions of linear and non-linear transport in the (L, F_d) plane. Rich static and dynamic visualizations of the vortex matter in different drive regimes supplement the quantitative results obtained.

I. INTRODUCTION

Point, columnar, and planar quenched disorder serve as natural pinning centers for magnetic-flux lines in type-II superconductors[1]. Effective pinning action through material defects may be used to curb flux flow due to external electric current, thereby mitigating the associated Ohmic loss and leading to a significant decrease in sample resistivity[2–5]. Planar defects are commonly found in the form of twin boundaries in high-T_c cuprates such as $YBa_2Cu_3O_{7-x}$ (YBCO) and La_2CuO_4. Twin boundaries are formed in these materials as they undergo a tetragonal to orthorhombic structural phase transition during the oxidative cooling phase of synthesis[6,7].

Although twin boundaries naturally tend to occur as a mosaic of twins from one of two orthogonal families[8,9], it is possible to fabricate samples containing a single family of twin planes[3,5,10]. The work in this paper pertains to the latter. In the case of a single family of twin planes, the pinning effect of twin boundaries on flux lines is highly anisotropic[10–19], *i.e.*, it strongly depends on the angle between the magnetic field and the twin planes (that are both oriented along the crystallographic c axis). Early experiments exploring this variation of pinning strength with field orientation yielded contradictory results[2,20], with later experiments[11] conclusively showing that pinning is strongest when the field is parallel to the twin planes and the current is flowing in the *ab* plane parallel to the twins thus exerting a Lorentz force on the flux lines perpendicular to the planar defects, confirming the results first presented by Kwok *et al.*[2,21] Experiments on flux-boundary pinning can be broadly classified into two types – those that measure electrical transport properties of the system such as resistivity and critical depinning current, and those where the flux lines are directly imaged via techniques like small angle neutron scattering[22] and scanning tunneling microscopy[23]. In transport experiments, planar defects are seen acting as strong pinning centers by their influence on the linear resistivity of a sample near the melting point of the Abrikosov lattice into a flux liquid. The monotonic increase of resistivity with temperature observed in the absence of planar (or other correlated) disorder in the sample is interrupted in the presence of defect planes by a sharp drop near the lattice melting transition which is attributed to strong pinning of vortices by the twin boundaries in the hexatic or liquid phase[2,24]. Experiments measuring the critical depinning current density J_c in systems with planar defects also confirm the strong flux-boundary pinning hypothesis, with a sharp maximum in J_c observed as a function of temperature just below the melting point of the Abrikosov lattice in a phenomenon known as the *peak effect*[25]. Real-time imaging experiments of flux lines driven perpendicular to a single family of twin planes also show strong pinning of magnetic vortices at the twin boundaries[26–28]. However, relatively recent experiments utilizing scanning superconducting quantum interference device microscopy to probe vortex motion near twin boundaries in pnictide superconductors show that vortices avoid pinning to twin boundaries in these materials owing to enhanced superfluid density near the boundaries, instead preferring to move parallel to them; this flux-boundary repulsion is offered as a possible explanation for the enhanced critical currents observed in twinned superconductors[29].

Numerical studies of vortex behavior in the presence of planar defects range from solving the full time-dependent Ginzburg-Landau equations[30–33] to more approximate

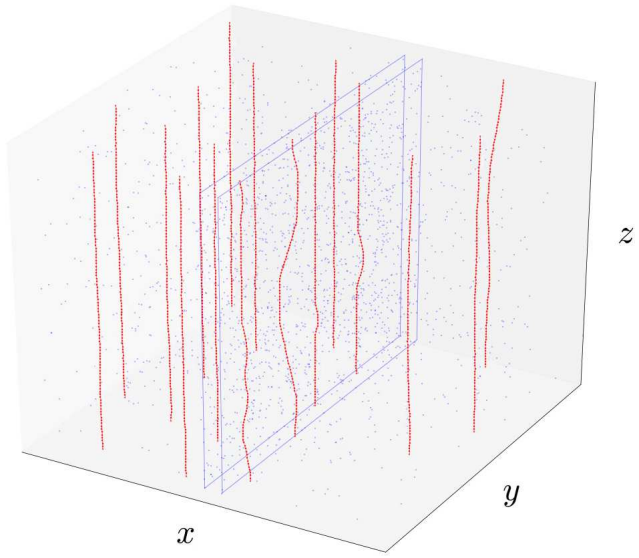

FIG. 1: Simulation snapshot of flux lines (red) driven along the x axis in the presence of two planar defects (blue) oriented perpendicular to the direction of drive and many randomly positioned point defects (blue).

descriptions[34–38] of vortices in two-dimensional thin-film and three-dimensional bulk samples as structureless point- or string-like objects that are studied with either Monte Carlo simulations or Langevin dynamics methods. The experimentally detected anisotropy of pinning and transport has been observed in numerical simulations of twinned superconductors[39,40] with thermal fluctuations being enhanced and vortex motion being facilitated within defect planes. Reichhardt *et al.* identified three phases of flux flow in London-Langevin studies of driven vortices subject to planar pinning, *viz.* guided plastic flow at low drives characterized by partially ordered vortices, highly disordered plastic flow at intermediate drives, and elastic flow at high drives with the vortices reordering into a lattice in this phase[35]. This is in agreement with earlier results of Crabtree *et al.*[41] which were obtained by solving the time-dependent Ginzburg-Landau equations on a discrete grid. Recent anaytical works argue that for randomly placed parallel planar defects, the flux line lattice displays a novel planar glass phase with an exponential decay of long-range translational order as opposed to the algebraic decay seen in the case of the Bragg glass obtained in the absence of planar defects[42–44]. Marchetti and Vinokur in their analytical studies of the low-temperature dynamics of magnetic flux lines in type-II superconductors, find that flux lines driven transverse to a family of parallel twin planes do so in a manner analogous to the motion of one-dimensional charge carriers in a disordered semiconductor induced by an electric field, and discuss various linear and non-linear transport mechanisms for vortex motion that are associated with different flux line excitations in the system[45,46].

In the present work, we use an elastic line description of vortices in a three-dimensional sample modeled to mimic the behavior of flux vortices in the mixed phase of YBCO. The elastic lines are mutually repulsive and are subject to a horizontal drive representing the Lorentz force exerted by an external current. The sample contains two planar defects perpendicular to the direction of drive as well as many randomly distributed point-like pinning sites that represent point disorder such as those produced by oxygen vacancies (FIG. 1). The dynamics of this model are simulated by numerically solving overdamped Langevin equations that account for the fast degrees of freedom in the system as stochastic forcing that is subject to certain physical constraints. This particular implementation of the elastic line model named LineMD was previously used by Dobramysl *et al.*[47] to study relaxation and aging phenomena of flux lines in the presence of point-like and columnar disorder. Since then, it has been employed to investigate relaxation dynamics of vortex lines following magnetic field, temperature and drive quenches[48–50], as well as the pinning time statistics for flux lines in disordered environments[51]. We have extended this work to here address the dynamics of vortices driven parallel to the x axis, and perpendicular to two parallel planar defects that are placed either a short distance (16 pinning center radii b_0) apart or a large distance ($160b_0$) apart. The system is periodic in the x direction and therefore the planar defect pair configuration employed here is comparable to a long YBCO sample containing evenly spaced pairs of parallel twin boundaries. We observe the long-time steady-state behavior of this system of flux lines for various sample thicknesses and drive strengths. These observations involve measuring several physical attributes and occurrence statistics for different flux line excitations as well as static and dynamic visualizations of the system under a range of conditions and from a number of (both two- and three-dimensional) perspectives.

The characterization of the depinning process, by which magnetic vortices subject to planar pinning transition from the pinned to the moving lattice state, has been greatly enhanced by direct measurements of the unique vortex excitations that emerge from planar defect-induced elastic deformations of these vortices. These measurements are made possible by the full three-dimensional specification of our simulated model coupled with the structural simplicity of the infinitesimally thin elastic lines that represent the vortices. The steady-state results pertaining to the depinning region reveal a rich assortment of drive (F_d) regimes, starting from an extremely disordered moving liquid at the onset of depinning that is followed by three more distinct regimes of increasing translational order that culminate in the dynamical freezing of the vortices into a moving triangular lattice. The excitation measurements complement these results by providing us with an insight into the types of structures that facilitate the realization of the different depinning regimes. The sample thickness (L) variation we have explored in this work establishes a strong depen-

dence of the manifestation of these novel regimes on the length of the flux lines.

The organization of this paper is as follows. The subsequent section explains the various terms in the Hamiltonian for our elastic line model, describes the Langevin Molecular Dynamics algorithm we employ to implement its stochastic dynamics, and specifies the material parameters we use for the implementation. This Section also covers definitions of the six observable quantities we measure directly and the simulation protocol we use to evolve the system to the steady state. We discuss the relevant results in Section 3, including the different regimes of flux flow observed as systems of vortex lines of varying length are driven from the pinned state at low drive values to the moving lattice state at sufficiently high drives. We focus on a discussion of the various flux line excitations observed in the different drive regimes and the separation of linear and non-linear phases of current-voltage response in the (L, F_d) plane that is delineated using quantitative excitation population data. We conclude the paper by summarizing our results in Section 4.

II. ELASTIC LINE MODEL AND SIMULATION PROTOCOL

A. Model Hamiltonian

We model flux lines as mutually repulsive elastic lines[52,53] in the extreme London limit, *i.e.*, when the London penetration depth is much larger than the coherence length. The Hamiltonian of the system is a sum of four terms, *viz.* the elastic line tension energy, the attractive potential due to pinning sites, the repulsive pair interactions between vortex line elements, and the work done by the external electric current:

$$H[\mathbf{r}_i] = \sum_{i=1}^{N} \int_0^L dz \left[\frac{\tilde{\epsilon}_1}{2} \left| \frac{d\mathbf{r}_i(z)}{dz} \right|^2 + U_D(\mathbf{r}_i(z)) + \frac{1}{2} \sum_{j \neq i}^{N} V(|\mathbf{r}_i(z) - \mathbf{r}_j(z)|) - \mathbf{F_d} \cdot \mathbf{r}_i(z) \right]. \quad (1)$$

$\mathbf{r}_i(z)$ represents the position vector in the xy plane of the line element of the ith flux line (one of N), at height z. The elastic line stiffness or local tilt modulus is given by $\tilde{\epsilon}_1 \approx \Gamma^{-2}\epsilon_0 \ln(\lambda_{ab}/\xi_{ab})$ where $\Gamma^{-1} = M_{ab}/M_c$ is the effective mass ratio or anisotropy parameter. λ_{ab} is the London penetration depth and ξ_{ab} is the coherence length, in the ab crystallographic plane. The in-plane repulsive interaction between any two flux lines is given by $V(r) = 2\epsilon_0 K_0(r/\lambda_{ab})$, where K_0 denotes the zeroth-order modified Bessel function. It effectively serves as a logarithmic repulsion that is exponentially screened at the scale λ_{ab}. The pinning sites are modeled as smooth potential wells, given by

$$U_D(\mathbf{r}, z) = -\sum_{\alpha=1}^{N_D} \frac{b_0}{2} p \left[1 - \tanh\left(5 \frac{|\mathbf{r} - \mathbf{r}_\alpha| - b_0}{b_0} \right) \right] \times \delta(z - z_\alpha), \quad (2)$$

where N_D is the number of pinning sites, $p \geq 0$ is the pinning potential strength, b_0 is the width of the potential well, while $\mathbf{r}_\alpha$ and z_α respectively represent the in-plane and vertical position of pinning site α. The Lorentz force exerted on the flux lines by an external current $\mathbf{j}$ is modeled in the system as a tunable, spatially uniform drive $F_d = |\mathbf{j} \times \phi_0 \mathbf{B}/B|$ in the x direction.

In the following, all lengths are measured in units of b_0 while energies are measured in units of $\epsilon_0 b_0$, where $\epsilon_0 = (\phi_0/4\pi\lambda_{ab})^2$ is the elastic line energy per unit length, and $\phi_0 = hc/2e$ is the magnetic flux quantum.

B. Langevin Molecular Dynamics

We simulate the dynamics of the model by discretizing the system along the direction of the external magnetic field (z direction) into layers. Consecutive layers are separated by c_0, *i.e.*, one crystal unit cell size along the crystallographic c direction[53,54]. Consequently, each elastic line consists of elastically coupled points, with each discrete element residing in a unique layer. The pinning sites (2) are also confined to these layers. The interactions between these discrete elements are encapsulated in the properly discretized version of the Hamiltonian (1) that we use to obtain coupled overdamped Langevin equations which we then solve numerically:

$$\eta \frac{\partial \mathbf{r}_i(t,z)}{\partial t} = -\frac{\delta H[\mathbf{r}_i(t,z)]}{\delta \mathbf{r}_i(t,z)} + \mathbf{f}_i(t,z). \quad (3)$$

Here, $\eta = \phi_0^2/2\pi\rho_n c^2 \xi_{ab}^2$ is the Bardeen-Stephen viscous drag parameter, where ρ_n represents the normal-state resistivity of YBCO near T_c[1,55]. We model the fast, microscopic degrees of freedom of the surrounding medium by means of thermal stochastic forcing as uncorrelated Gaussian white noise $\mathbf{f}_{i,z}(t)$ with vanishing mean $\langle \mathbf{f}_{i,z}(t) \rangle = 0$. Furthermore, these stochastic forces obey the Einstein relation

$$\langle \mathbf{f}_{i,z}(t) \cdot \mathbf{f}_{j,z'}(s) \rangle = 4\eta k_B T \delta_{ij} \delta_{zz'} \delta(t - s),$$

which ensures that the system relaxes to thermal equilibrium with a canonical probability distribution $P[\mathbf{r}_{i,z}] \propto e^{-H[\mathbf{r}_{i,z}]/k_B T}$ in the absence of any external current.

C. Model Parameters

We have selected our model parameters to closely match the material properties of the ceramic high-T_c type-II superconductor YBCO. The pinning center radius

is set to $b_0 = 35\mathring{A}$. The inter-layer spacing in the crystallographic c direction is set to $c_0 = b_0$. The in-plane London penetration depth and superconducting coherence length are chosen to be $\lambda_{ab} = 34b_0 \approx 1200\mathring{A}$ and $\xi_{ab} = 0.3b_0 \approx 10.5\mathring{A}$ respectively, in order to represent YBCO, which has a high effective mass anisotropy ratio $\Gamma^{-1} = 1/5$. The line energy per unit length is $\epsilon_0 \approx 1.92 \cdot 10^{-6}$erg/cm. This effectively renders the vortex line tension energy scale to be $\tilde{\epsilon}_1/\epsilon_0 \approx 0.189$. The pinning potential well depth is taken as $p/\epsilon_0 = 0.05$. The temperature in our simulations is set to 10 K ($k_{\rm B}T/\epsilon_0 b_0 = 0.002$ in our simulation units). The Bardeen–Stephen viscous drag coefficient $\eta = \phi_0^2/2\pi\rho_n c^2 \xi_{ab}^2 \approx 10^{-10}\,\mathrm{erg \cdot s/cm^2}$ is set to one, where $\rho_n \approx 500\,\mu\Omega$m is the normal-state resistivity of YBCO near T_c[56]. This results in the simulation time step being defined by the fundamental temporal unit $t_0 = \eta b_0/\epsilon_0 \approx 18$ ps; simulation times are measured in units of t_0.

D. Measured Quantities

Our understanding of the system is primarily developed by examining certain physical observables. One such observable is the mean velocity v of the vortex lines,

$$\mathbf{v} = \left\langle \frac{d}{dt}\mathbf{r}_i(z) \right\rangle . \tag{4}$$

Here, $\langle \ldots \rangle$ represents an average over all line elements of line i as well as an average over all N lines and different realizations of the disorder and the noise.

Another quantity of interest is the mean *radius of gyration*,

$$r_g = \sqrt{\langle (\mathbf{r}_i(z) - \langle \mathbf{r}_i \rangle)^2 \rangle} \ , \tag{5}$$

i.e., the standard deviation of the lateral positions $\mathbf{r}_i(z)$ of the points constituting the ith flux line, averaged over all the lines. r_g is a measure of overall roughness of the lines in the system.

The third quantity we measure is the *fraction of pinned line elements*, defined as

$$f_p = n(r < b_0)/n_{\rm total}. \tag{6}$$

Here, $n(r < b_0)$ is the number of line elements located at a distance r from a pinning site that is less than one pinning center radius b_0. $n_{\rm total}$ is the total number of line elements in the system. Thus, f_p is the fraction of line elements in the system that are located within distance b_0 of an attractive defect site.

We also measure the numbers of different flux line excitations that appear in the system, *viz. half-loops*, *single kinks* and *double kinks* (FIG. 2). A flux line forms a half-loop (FIG. 2a) when it becomes partially depinned from a defect plane and the separation between the depinned portion and the plane is smaller than the inter-planar distance. A single kink (FIG. 2b) appears when part of a line is trapped in one defect plane while an adjacent section is trapped in the neighboring plane. A double kink (FIG. 2c) is similar to a half-loop but with a larger separation between the depinned portion and the remainder of the flux line that results in the outermost portion of the half-loop being pinned to the next defect plane; this can also be viewed as a specific combination of two single kinks and is accounted for as such in our measurements. In each simulation run, we record the total number of each type of vortex excitations appearing in the system (which of course depend on the total number of flux lines N). We have used $N = 16$ vortices in all of the work presented in this study.

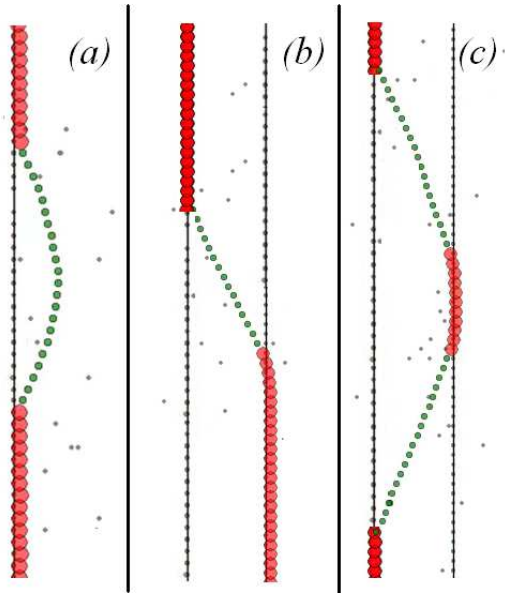

FIG. 2: Simulation snapshots of the system projected onto the xz plane for a side view, showing flux lines forming three different excitations: (a) half-loop, (b) single kink, and (c) double kink. The green dotted lines are flux lines, the gray dots represent point pins, and the black vertical lines planar defects. The red dotted sections are those portions of the flux lines that are trapped at planar defects. The drive F_d is oriented along the positive x (right) direction.

E. Simulation Protocol

We obtain steady-state results for our system via the following procedure. We set the sample thickness of the system (in the z direction) L to the desired value and initialize it with two planar defects oriented perpendicular to the direction of the drive (x direction). Each planar defect consists of rows of point defects extending along the entire height of the system. Each row of point defects extends along the length of the system in the y direction, and consecutive defects are separated by a distance of $2\,b_0$. We set up our pair of defect planes

in one of two configurations – either close together, *i.e.*, where the planes are separated by $16\,b_0$ ($\sim 5\%$ of the system extension in the x direction) or far apart with a separation of $160\,b_0$ ($\sim 50\%$ of the system length in the x direction). Besides the two defect planes, point defects are randomly distributed throughout the system to maintain a concentration of 1116 defects per plane. The random point defects provide the effective viscocity experienced by moving flux lines in a real physical system. We employ periodic boundary conditions in the x and y directions and free boundary conditions in the z direction. We set the horizontal system size (in the xy plane) to $(16/\sqrt{3}\lambda_{ab})b_0 \times 8\lambda_{ab}b_0$. This ratio of horizontal boundary lengths is necessary to ensure that the flux lines can equilibrate to a periodic hexagonal Abrikosov lattice in the absence of disorder.

We randomly place $N = 16$ straight flux lines in the system and immediately subject them to an effective temperature of $0.002\,\epsilon_0 b_0/k_B$ and the desired drive strength F_d. The lines are allowed to relax in this constant temperature-drive bath for an initial relaxation time of $100,000\,t_0$. At this point, we start measuring the various observables in the system every 100 time steps, a duration larger than the correlation times in the system that range from $20\,t_0$ to $45\,t_0$ depending on the strength of the applied driving force. We perform 1000 such measurements and under the ergodic assumption, record their average for each observable. We simulate 10 independent realizations in this manner and perform an ensemble average over these realizations. Between the time averaging and ensemble averaging, we thus average each data point over 10,000 independent values.

III. RESULTS

A. The Six Dynamical Drive Regimes

We have performed a detailed study of the long-time steady-state behavior of vortex matter subject to randomly placed point pins and two parallel extended planar defects oriented perpendicular to the drive as a function of drive for several sample thicknesses ($L = 50\,b_0$ to $250\,b_0$). These steady-state curves reveal new distinct drive regimes not observed in our prior studies[47,49] with point-like and columnar defects, and underscore the much richer kinetics accessible with this defect geometry.

For the case where the planar defects are placed close together, we observe six drive regimes in total – a *pinned* and a *moving-lattice* regime found respectively at the beginning and end of the drive spectrum under study, along with four intermediate regimes that populate the remarkably wide depinning transition region connecting the two extremal regimes. These intermediate regimes are the *liquid regimes I* and *II*, a *smectic*, and a *hexatic* regime[57] (see FIG. 3). The defining features of each regime and the mechanisms by which the system subsequently evolves into each of these regimes are described below.

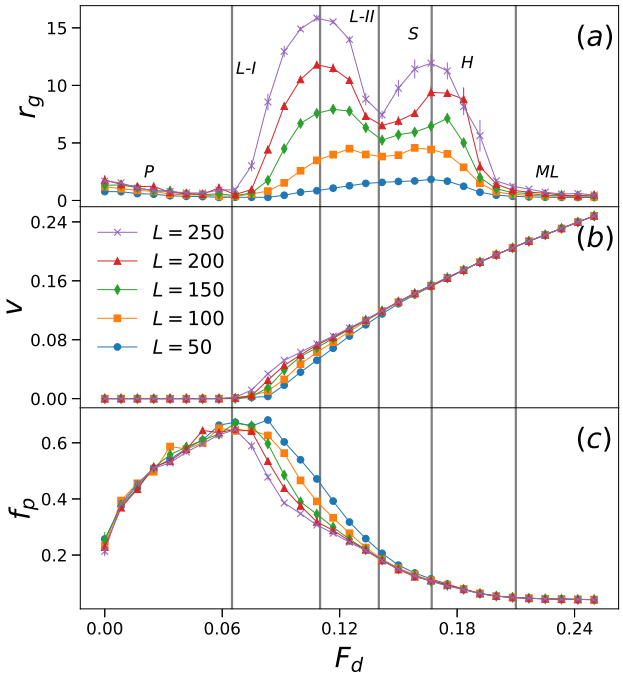

FIG. 3: Steady-state (a) radius of gyration r_g (units of b_0), (b) mean vortex velocity v (units of b_0/t_0), and (c) fraction of pinned line elements f_p as a function of drive F_d (units of ϵ_0) for interacting flux lines in the presence of two closely placed planar defects, in samples of varying sample thickness L (units of b_0). For $L = 250\,b_0$, vertical gray lines are used to demarcate the six drive regimes, that are labeled with acronyms – P: pinned regime, L-I: liquid regime I, L-II: liquid regime II, S: smectic regime, H: hexatic regime and ML: moving lattice regime. Here and in the following figures only error bars larger than the symbol sizes are shown.

The first drive regime in the system represents the pinned state; it is characterized by a very low ($< 3\,b_0$) mean radius of gyration r_g, zero mean velocity, v and a sizable non-zero fraction of pinned line elements f_p (pinning fraction) that actually grows monotonically with drive (FIG. 3). In this regime, a proportion of the flux lines are trapped in the first planar defect (the one with the lower x coordinate) while the remainder of them are held stationary at a fixed distance behind them by the externally applied drive and the opposing long-range inter-vortex repulsions (see FIG. 4a1 and FIG. 4a2). Due to the vertically correlated configuration of the planar defects, the flux lines trapped within them are nearly perfectly straight and therefore display a low radius of gyration. Those lines not trapped by planar defects are also quite straight on account of not only their intrinsic elastic line tension but also the repulsive caging induced by the plane-trapped lines positioned in front of them. This results in the low overall gyration radius and zero mean velocity we observe in the steady state. The system in the pinned regime is a destabilized Bragg glass display-

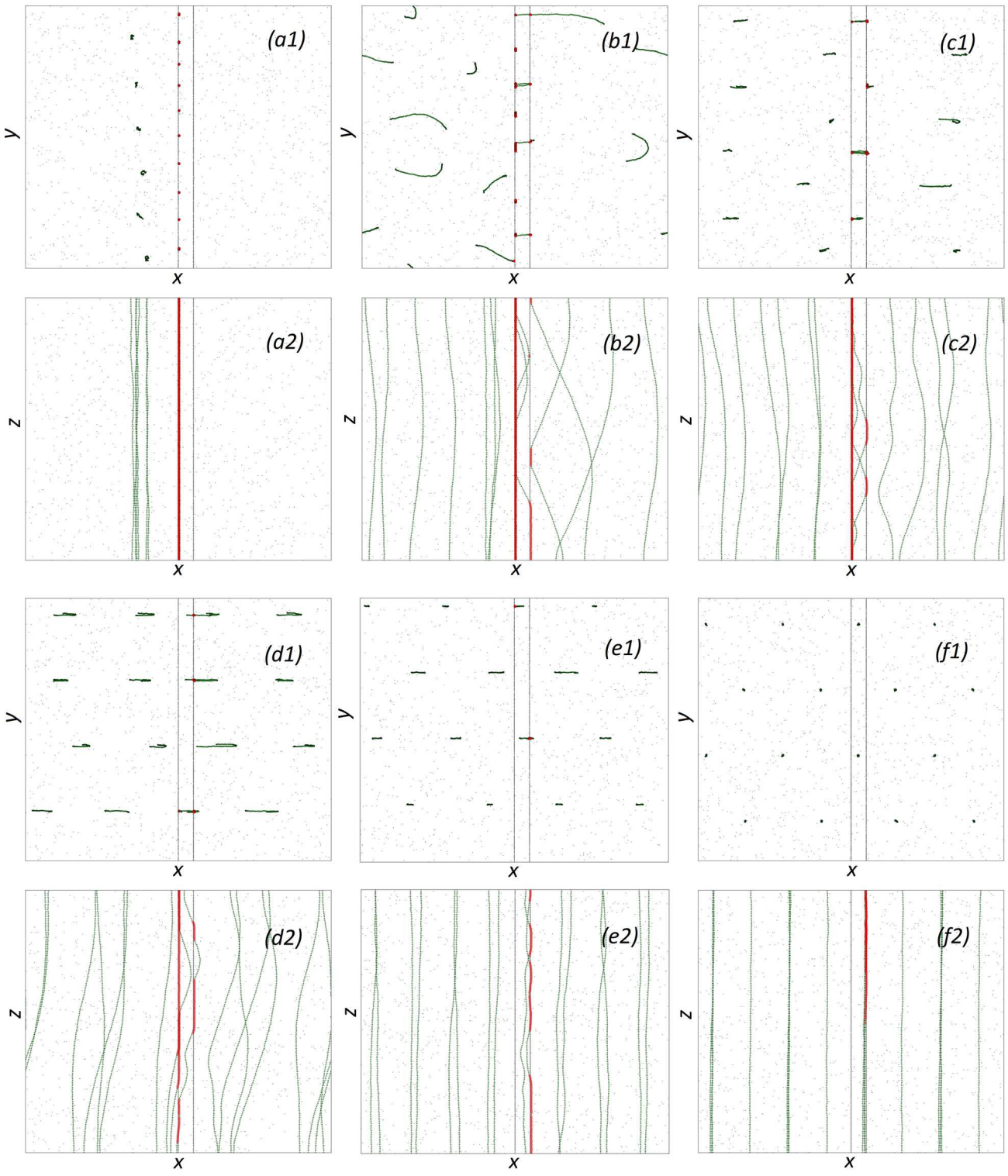

FIG. 4: Simulation snapshots of a system with 16 flux lines in a sample of thickness $L = 150\,b_0$, in the presence of two closely placed planar defects, projected onto the (1) xy plane for a top view, and (2) xz plane for a side view in the (a) pinned, (b) liquid I, (c) liquid II, (d) smectic, (e) hexatic, and (f) moving lattice regimes of drive. The (green) dotted lines represent the vortices, and the black vertical lines are planar defects. The red dotted sections mark those portions of the flux lines that are trapped at planar defects. The drive F_d is oriented in the positive x (right) direction. The system boundary lengths in the x and y directions are $314\,b_0$ and $272\,b_0$, respectively. The full videos from which these snapshots have been taken can be viewed at `https://figshare.com/s/8a1e4bf34f463f988ebd`.

ing quasi long-range positional order as seen in FIG. 4a1. Within the pinned regime, higher drives correspond to higher pinning fractions since an increase in drive shrinks the distance between the free-standing caged vortices and those trapped in the first defect plane, thereby increasing the susceptibility of a free-standing flux line to be pulled into the first defect plane. In this regime the influence of sample thickness L on all of the measured quantities is negligible, with the steady-state curves for different L appearing identical within our statistical errors. This is due to the fact that in the pinned regime, the flux lines are virtually motionless barring thermal fluctuations. The influence of the length of the flux lines only becomes appreciable once we enter one of the moving regimes where the flux lines start experiencing partial pinning by the planar defects; this affects lines of different lengths quite differently, as described in detail below.

Increasing the drive further, we exit the pinned regime to enter the liquid regime I, the first of four regimes that comprise the depinning transition region. In this regime, the drive is strong enough for the flux lines to detatch from the planar defects, while suffering large distortions (FIG. 4b1 and FIG. 4b2) that result in a sharp increase in their mean gyration radius (FIG. 3a). The incipient vortex motion also results in the mean vortex velocity assuming non-zero values (FIG. 3b). Both gyration radius and velocity increase monotonically with drive, while the pinning fraction diminishes (FIG. 3c) on account of fewer line elements being pinned as we increase the drive and go deeper into the depinning region. The increased drive in this regime transforms the earlier Bragg glass into a moving liquid that is practically devoid of long-range translational order (FIG. 4b1). This moving liquid phase of the system spans two drive regimes, the liquid regimes I and II. The crossover from the pinned into the liquid regime I occurs at lower drives for thicker samples (greater L) than for thinner ones since longer vortex lines have a larger number of points along their trajectory which can potentially be set free from the defect plane holding them, by the applied drive with assistance from thermal fluctuations. This increases the probability of neighboring line elements to break free as they are elastically coupled to the first detached element, inducing a cascading effect whereby the entire line is pulled free from the defect plane. For any given drive in this regime, longer flux lines, *i.e.*, those in thicker samples (with greater L), display a larger gyration radius (FIG. 3a), as longer lines are capable of incorporating larger distortions as they are pulled free from the defect planes at different locations along their length by the drive. The opposite trend is true for the pinning fraction f_p (FIG. 3c), with shorter lines being more likely than longer ones to be trapped by planar defects. The propensity to be partially depinned also results in longer lines moving faster than shorter ones on average (FIG. 3b) as their motion is not impeded by the disorder as much.

Following the liquid regime I, we enter the second transition regime, the liquid regime II, where the stronger external forcing propels the flux lines faster through the defect planes, as seen in the rising velocity-drive curves (FIG. 3b) for all sample thicknesses L. The faster velocity means the lines spend less time at the pinning sites (both planar and point) which reduces the distorting effects of the disorder on the vortices, resulting in comparatively straighter flux lines (FIG. 4c2). This is evident in the decline of the gyration radius with drive in this regime compared to its upward trend in the previous regime (FIG. 3a). The peak in gyration radius that marks the change in regimes occurs at different points in systems with different L, with thicker samples crossing over at lower drive values than thinner samples. The pinning fraction continues to decline with drive in this regime albeit at a slower rate than in the previous regime (FIG. 3c).

The next regime is the smectic regime. This is the dynamical regime unique to the system under consideration (two planar defects close together and perpendicular to the drive) and has not appeared in systems populated by only point or columnar defects. The gyration radius instead of monotonically decreasing with drive after undergoing its first maximum, as in systems containing only point or columnar defects, once again starts to increase at a certain drive strength (FIG. 3a), which marks the start of the third intermediate regime. This anomalous behavior can be explained on the basis of three factors: high line velocity, a finite periodic system, and repulsive vortex interactions. As we enter the third intermediate regime, the lines are moving faster than in previous regimes on account of the higher driving force (FIG. 3b). The enhanced speed leads to a relatively short time period between a flux line leaving the second defect plane and re-encountering the first one after crossing the periodic boundary in the x direction. As a result, any major line distortion, such as a tilt in vertical orientation effected by the asymmetric depinning of a flux line from the second defect plane starting at one end of the line, has insufficient time to relax before it is quickly reinforced by the rapidly approaching first defect plane (FIG. 4d). The long-range inter-line repulsions propagate these aberrations to neighboring lines, significantly enhancing the overall distortive effect. In the smectic regime, the moving vortex liquid starts developing transverse order to form a moving smectic phase that is characterized by well-defined horizontal channels of flux flow (FIG. 4d1). This marks the beginning of the dynamic freezing process that finally culminates in the flux lines forming a moving vortex lattice. The growing gyration radius characteristic of the smectic regime is far more pronounced in longer lines than shorter ones owing to the greater capacity of the former for containing horizontally wide-spanning structures. In fact, for flux lines with $L < 100\, b_0$, the effect is insignificant enough that the gyration radius simply does not form the valley which signifies the transition from the liquid regime II to the smectic regime, instead growing monotonically until its eventual degradation in the hexatic regime as the

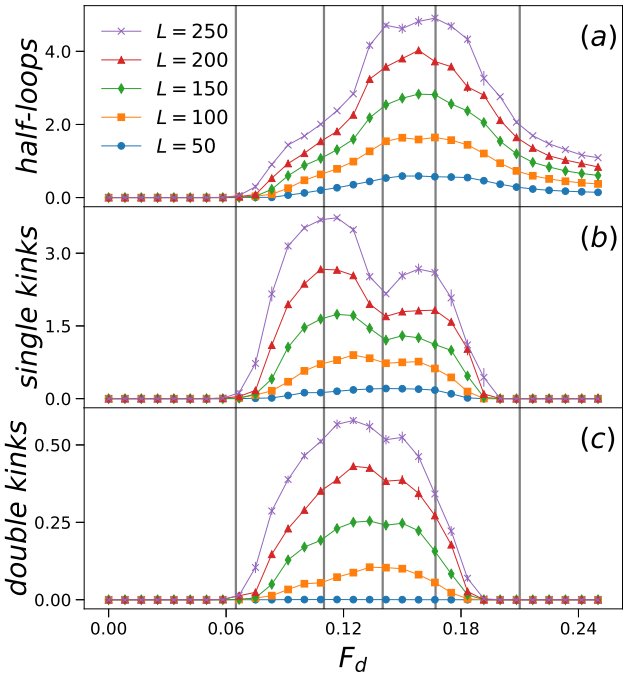

FIG. 5: Steady-state number of (a) half-loops, (b) single kinks, and (c) double kinks as a function of drive F_d (units of ϵ_0) for interacting flux lines in the presence of two closely placed planar defects, in samples of varying sample thickness L (units of b_0). The six drive regimes corresponding to $L = 250\, b_0$ are demarcated by vertical gray lines.

vortices dynamically freeze into a triangular lattice. Essentially, these shorter flux lines transition directly from the liquid regime I to the hexatic regime, bypassing the liquid II and smectic regimes.

Once the driving force crosses a certain threshold ($\sim 0.17\,\epsilon_0$), the attractive influence of the planar defects becomes sufficiently weak that they are no longer capable of either inducing large distortions in the flux lines or reinforcing them. This threshold marks the beginning of the fourth and final depinning transition regime, the hexatic regime, where the flux lines start to arrange in a distorted triangular lattice (FIG. 4e1). The evolution of the system with drive in this regime is qualitatively similar to that in the liquid regime II, *i.e.*, gyration radius (FIG. 3a) and pinning fraction (FIG. 3c) decrease as a function of drive as the flux lines become faster (FIG. 3b), straighter (FIG. 4e2), and less susceptible to pinning. We also observe progression in the dynamic freezing process, with the flux lines starting to arrange themselves into a triangular lattice, albeit an imperfect one, that suffers from the distortive effects of the relatively weaker but still potent pinning centers, especially the planar defects. The role of the sample thickness L is also diminished in this high-drive regime, as partial pinning of flux lines occurs less frequently due to the effectively reduced pinning strength of the defects, resulting in the steady-state curves for various L starting to converge as we move to higher drives.

The final drive regime in the series is the moving lattice regime. The drive is sufficiently strong that the pinning at the attractive defects is negligible, and the lines are once again almost perfectly straight as in the low-drive pinned regime (FIG. 4f2). With the destabilizing influence of disorder effectively removed, the flux lines arrange themselves into a moving hexagonal Abrikosov lattice (FIG. 4f1), completing the dynamic freezing process. The mean velocity of the lines shows a linear dependence on drive strength, indicating that the system has entered an Ohmic regime with linear I-V characteristics (FIG. 3b). The pinning fraction (FIG. 3c) plateaus a little above zero ($f_p \approx 0.04$) as does the gyration radius (FIG. 3a), as the lines move practically freely through the system without the pinning and roughening effects of the defects. The role of sample thickness diminishes further, with the velocity and pinning fraction curves for different L coinciding perfectly for the entire width of the regime, and those for the gyration radius doing so near the very end of the drive spectrum under consideration.

B. Flux Line Excitations

In order to better understand the line structures that characterize the novel regimes observed in our studies of vortex matter subject to planar defects, we devised a technique of directly measuring the flux line excitations, *viz.* half-loops, single kinks and double kinks, that appear in our system due the interactions of the flux lines with the closely placed defect planes (see Section II D for definitions).

The two local gyration radius maxima (FIG. 3a) that mark the drive regime transitions respectively from the liquid regime I to II and smectic to hexatic coincide exactly with corresponding peaks in the single-kink (FIG. 2b) steady-state curves (FIG. 5b). This observation along with the overall structural similarity between the gyration radius and single-kink steady-state data suggests that single kinks are the primary drivers of flux line distortion. For any given driving force, we see a positive correlation between the number of single kinks and vortex length (or sample thickness) L – the longer a flux line, the more potential points there exist along its length where a kink might form. This correlation between line length and mean number of steady-state excitations holds true for the other line structures (half-loops and double kinks) under consideration as well.

Vortex half-loops (FIG. 2a) occur in the system with a frequency comparable to that of single kinks and attain a maximum at the transition point between the smectic and hexatic drive regimes (FIG. 5a). In contrast to single kinks, the formation of half-loops requires the flux lines to be relatively straight. We thus observe a steady increase in the number of half-loops beyond the pinned regime as the lines that start out distorted in the liquid regime

I, steadily straighten out with increasing drive until the start of the the hexactic regime regime, where the number of half-loops peaks. Beyond this regime, the pinning influence of the planar defects starts to wane in comparison to the relatively high drive, and we see the number of half-loops monotonically decline with drive. It is worth noting that of the three types of excitations under study, half-loops are the most resilient structures in the system, with their population being significantly above zero ($0.2 \sim 0.5$) in the moving lattice regime, even though single kinks (FIG. 5b) and double kinks (FIG. 5c) practically stop appearing in the system well before the onset of this regime. This is consistent with the theoretical findings of Marchetti and Vinokur that for large enough current, half-loop configurations of transverse width smaller than the average separation between the planes are the dominant excitations[45,46].

Double kinks (FIG. 2c) occur far less frequently (FIG. 5c) than single kinks or half-loops as they require a flux line to assume a spatial structure of relatively higher complexity. Qualitatively speaking, the double-kink steady-state curves share more in common with those for single kinks than half-loops, with the major double-kink peak occurring in the middle of the liquid regime II, a slightly but noticeably higher drive value than that corresponding to the major single-kink peak, which occurs at the beginning of liquid regime II. For, as the flux lines evolve from their most distorted shape at the outset of liquid regime II to being somewhat straighter by the end of this regime, the formation of double kinks is facilitated as these vortices start to *loop back* on themselves and reattach to the first defect plane.

C. Widely Spaced Defect Planes

When we increase the distance betwen the planar defects to 50% of the system length, the richness and variety of the depinning regimes observed for closely placed planes is diminished significantly. The flux lines of all lengths under consideration, except for the longest ($L = 250\, b_0$), are too short to allow for the formation of single-kink (FIG. 6b) or double-kink excitations. As a result, for shorter samples ($L < 150\, b_0$), the single-kink driven gyration radius *valley* (comprised of the liquid II and smectic regimes) separating the liquid regime I and the hexatic regime practically disappears (FIG. 6a), and we end up with a flux flow profile resembling that for a system with columnar defects, *i.e.*, containing a single maximum in the steady-state gyration radius curve that marks the transition of the system directly from the liquid to the hexatic phase in the depinning region. For all sample thicknesses considered, the only flux line excitations to appear in any appreciable quantity are half-loops (FIG. 6c), since they need just one defect plane to form.

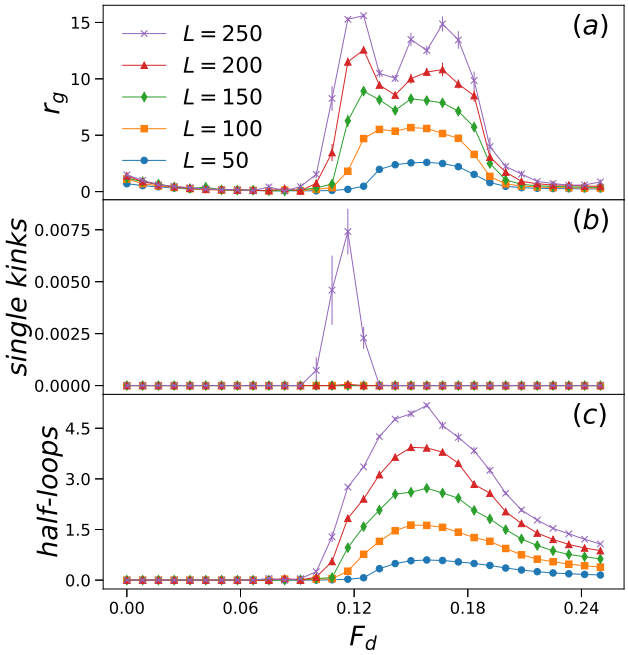

FIG. 6: Steady-state (a) radius of gyration (units of b_0), (b) number of half-loops, and (c) number of single kinks as a function of drive F_d (units of ϵ_0) for interacting flux lines in the presence of two widely spaced planar defects, in samples of varying sample thickness L (units of b_0).

D. Transport Regimes

The different flux line excitations discussed in the preceding Section are associated with different transport mechanisms for the vortices to move through the system. These mechanisms may be classified as linear or non-linear depending on whether they result in a linear or non-linear current-voltage response in the sample. Our investigation of transport regimes is primarily motivated by the analytical works by Marchetti and Vinokur[45,46] on dilute vortex arrays. These sources provide the context for the results we report in this subsection as well as the definitions included herein. Marchetti and Vinokur discuss five transport regimes in all, of which we are able to observe three in our system as a consequence of our limiting the number of planar defects in our simulations to two. These regimes are: the linear *rigid flow* regime for very thin samples; the linear *nearest-neighbor hopping* regime for thicker samples dominated by double kinks; and the non-linear *half-loop* regime dominated by half-loops that emerges in samples of all thicknesses.

Marchetti and Vinokur showed that there exists a characteristic current scale $J_L \sim 1/L$ that separates the regions of linear and non-linear current-voltage response in the (L, J) plane, where L is the sample thickness in the direction of the magnetic field, J is the electric current that exerts a Lorentz force (what we refer to as the drive

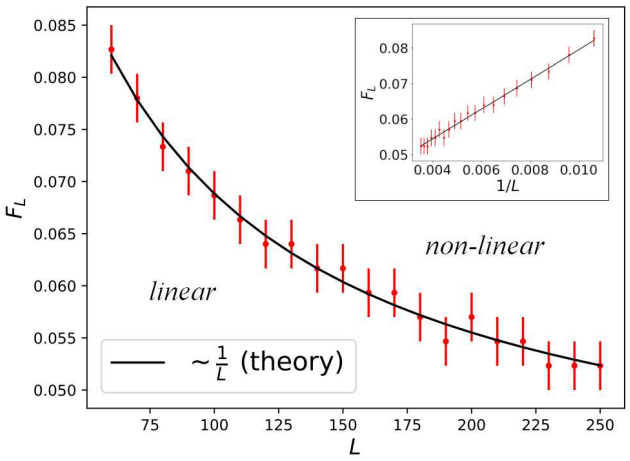

FIG. 7: Crossover drive strength F_L separating the regions of linear and non-linear response, as a function of sample thickness L. The inset displays F_L plotted as a function of $1/L$.

F_d) in the direction perpendicular to the defect planes (the x direction), and J_L is the critical current value, which if exceeded causes flux lines in a sample of thickness L to cross over from a linear to a non-linear transport regime. Since $J \sim F_d$, it follows that $F_L \sim 1/L$ where F_L is the critical drive corresponding to the critical current J_L. We have confirmed this relationship in our simulations (FIG. 7). The curve representing the cross-over boundary between the regimes of linear and non-linear response was obtained by identifying the critical drive strength F_L when the steady-state number of half-loops starts assuming non-zero values, and repeating this process for 21 systems of varying sample thickness, evenly-spaced between $L = 50\,b_0$ and $250\,b_0$.

IV. CONCLUSION

We have examined a system of driven flux lines in the presence of two planar defects aligned parallel to the magnetic field and perpendicular to the direction of drive. We probed the steady-state drive dynamics of the system over several sample thicknesses, and for closely placed defect planes, observed a number of interesting regimes of flux flow ranging from a quasi-ordered Bragg glass at the lowest drive strengths to a perfectly ordered moving lattice at the highest drive strengths, along with four intermediate regimes with vortex matter in different stages of disorder. This system is quite distinct in its dynamical signatures from samples with other types of quenched disorder such as point or randomly placed columnar defects. The depinning region in the flux flow profile is remarkably broad with non-trivial topology that we have characterized via novel methods of detecting and quantitatively analyzing the unique spatial structures or excitations assumed by the flux lines. These methods supplement the quantitative analysis of essential summary observables in the system, and furthermore are aided by rich visualizations of the vortex matter from different perspectives.

At drives close to zero, we see the system equilibrate in the steady state, to a destabilized Bragg glass phase (pinned regime) with quasi-long-range ordered flux lines either trapped in the first defect plane or held at a fixed distance behind this planar defect by the opposing forces of drive and mutual vortex repulsion. The influence of sample thickness or vortex length is negligible in this regime that is devoid of flux flow.

When the drive is increased beyond the range of the pinned regime, we see strongly disordered plastic vortex motion that is characterized by very high gyration radius or line roughness, non-zero line velocity, and a decline in pinning fraction. We call this the liquid regime I; the transition point from the pinned phase into this regime also marks the point when we observe a maximum number of single-kink excitations. Single kinks thus emerge as the dominant drivers of line distortion in the system, with half-loop and double-kink excitations acting as secondary sources of flux line roughening. Longer flux lines show enhanced distortion as well as excitations of all three kinds compared to shorter ones, owing to the greater number of points along their length that can be dislodged from pinning centers. Upon increasing the drive further, the gyration radius (and number of single kinks) attains a maximum, and then starts decreasing with drive, marking the onset of liquid regime II, a regime where drive strength dominates over the distortion-inducing effect of the planar defects, resulting in faster moving and straighter lines. A maximum number of double-kink excitations is observed in this regime.

Instead of monotonically continuing in this manner until the system reaches the moving lattice state (as samples with point or columnar defects would), the gyration radius experiences a minimum at the onset of the smectic regime, and starts to again increase with drive. Close examination of the flux line configurations reveals this *gyration radius valley* to be a consequence of the finite, periodic nature of the system, with major line distortions having insufficient time to relax before being reinforced by the *next* defect plane that lies beyond the periodic boundary along the drive direction. This phenomenon should be experimentally realizable in samples with evenly spaced pairs of parallel twin boundaries that are sufficiently long in the drive direction – we therefore do not dismiss this phenomenon as a mere finite-size effect without experimental significance. Just as with the transition from the liquid regime I to II, stronger drive pushes the system from the smectic regime to the hexactic regime, where the pinning strength becomes sufficiently weak compared to the driving force that it stops inducing the large destabilizing vortex distortions it induces in the smectic regime. Flux lines start becoming straighter and faster yet again, eventually forming a perfectly ordered moving triangular Abrikosov lattice marking the end of the dynamic freezing process and the termi-

nation of the hexatic regime. Finally, the system reaches the moving lattice regime where the steady-state curves for different sample thicknesses start to converge, indicating the diminishing influence of both flux line length and planar pinning.

Quantitative measurements of the flux line excitation populations were utilized to detect the phase boundary separating the regions of linear and non-linear current-voltage response in the (L, J) or (L, F_d) plane. By identifying the drive strength F_L corresponding to the emergence of half-loops in the system for each sample thickness L, we have confirmed that the critical drive strength F_L needed to push the system from a linear to a non-linear transport regime shows a $1/L$ dependence, as analytically predicted by Marchetti and Vinokur[46].

Acknowledgments

This research is supported by the U.S. Department of Energy, Office of Basic Energy Sciences, Division of Materials Sciences and Engineering under Award DE-FG02-09ER46613.

[1] G. Blatter, M. V. Feigel'man, V. B. Geshkenbein, A. I. Larkin, and V. M. Vinokur, Rev. Mod. Phys. **66**, 1125 (1994).

[2] W. K. Kwok, U. Welp, G. W. Crabtree, K. G. Vandervoort, R. Hulscher, and J. Z. Liu, Phys. Rev. Lett. **64**, 966 (1990).

[3] W. K. Kwok, S. Flesher, U. Welp, V. M. Vinokur, J. Downey, G. W. Crabtree, and M. M. Miller, Phys. Rev. Lett. **69**, 3370 (1992).

[4] S. Flesher, W. K. Kwok, U. Welp, V. M. Vinokur, M. K. Smith, J. Downey, and G. W. Crabtree, Phys. Rev. B **47**, 14448 (1993).

[5] G. W. Crabtree, W. K. Kwok, U. Welp, J. Downey, S. Flesher, K. G. Vandervoort, and J. Z. Lin, Physica C **185-189**, 282 (1991).

[6] M. Hervieu, B. Domenges, C. Michel, G. Heger, J. Provost, and B. Raveau, Phys. Rev. B **36**, 3920 (1987).

[7] W. W. Schmahl, A. Putnis, E. Salje, P. Freeman, A. Graeme-Barber, R. Jones, K. Singh, J. Blunt, P. Edwards, J. Loram, et al., Philos. Mag. Lett. **60**, 241 (1989).

[8] T. Roy and T. Mitchell, Philos. Mag. A **63**, 225 (1991).

[9] H. Safar, S. Foltyn, H. Kung, M. Maley, J. Willis, P. Arendt, and X. Wu, Appl. Phys. Lett. **68**, 1853 (1996).

[10] S. Fleshler, W.-K. Kwok, U. Welp, V. M. Vinokur, M. K. Smith, J. Downey, and G. W. Crabtree, Phys. Rev. B **47**, 14448 (1993).

[11] J. Liu, Y. Jia, R. Shelton, and M. Fluss, Phys. Rev. Lett. **66**, 1354 (1991).

[12] J.-H. Chu, J. G. Analytis, K. De Greve, P. L. McMahon, Z. Islam, Y. Yamamoto, and I. R. Fisher, Science **329**, 824 (2010).

[13] T. Friedmann, M. Rabin, J. Giapintzakis, J. Rice, and D. Ginsberg, Phys. Rev. B **42**, 6217 (1990).

[14] G. Dolan, F. Holtzberg, C. Feild, and T. Dinger, Phys. Rev. Lett. **62**, 2184 (1989).

[15] B. Roas, L. Schultz, and G. Saemann-Ischenko, Phys. Rev. Lett. **64**, 479 (1990).

[16] Y. Ando, K. Segawa, S. Komiya, and A. Lavrov, Phys. Rev. Lett. **88**, 137005 (2002).

[17] A. Raynes, S. Freiman, F. Gayle, and D. Kaiser, J. Appl. Phys. **70**, 5254 (1991).

[18] C. Villard, G. Koren, D. Cohen, E. Polturak, B. Thrane, and D. Chateignier, Phys. Rev. Lett. **77**, 3913 (1996).

[19] M. Turchinskaya, D. Kaiser, F. Gayle, A. Shapiro, A. Roytburd, V. Vlasko-Vlasov, A. Polyanskii, and V. Nikitenko, Physica C **216**, 205 (1993).

[20] L. Swartzendruber, A. Roitburd, D. Kaiser, F. Gayle, and L. Bennett, Phys. Rev. Lett. **64**, 483 (1990).

[21] U. Welp, W. Kwok, G. Crabtree, K. Vandervoort, and J. Liu, Appl. Phys. Lett. **57**, 84 (1990).

[22] M. Eskildsen, P. Gammel, B. Barber, A. Ramirez, D. Bishop, N. Andersen, K. Mortensen, C. Bolle, C. Lieber, and P. Canfield, Phys. Rev. Lett. **79**, 487 (1997).

[23] I. Maggio-Aprile, C. Renner, A. Erb, E. Walker, and Ø. Fischer, Phys. Rev. Lett. **75**, 2754 (1995).

[24] D. López, E. Righi, G. Nieva, F. De La Cruz, W. Kwok, J. Fendrich, G. Crabtree, and L. Paulius, Phys. Rev. B **53**, R8895 (1996).

[25] A. Larkin, M. C. Marchetti, and V. Vinokur, Phys. Rev. Lett. **75**, 2992 (1995).

[26] I. Maggio-Aprile, C. Renner, A. Erb, E. Walker, and O. Fischer, Nature **390**, 487 (1997).

[27] V. Vlasko-Vlasov, L. Dorosinskii, A. Polyanskii, V. Nikitenko, U. Welp, B. Veal, and G. Crabtree, Phys. Rev. Lett. **72**, 3246 (1994).

[28] C. Duran, P. Gammel, R. Wolfe, V. Fratello, D. Bishop, J. Rice, and D. Ginsberg, Nature **357**, 474 (1992).

[29] B. Kalisky, J. Kirtley, J. Analytis, J.-H. Chu, I. Fisher, and K. Moler, Phys. Rev. B **83**, 064511 (2011).

[30] G. Crabtree, D. Gunter, H. Kaper, A. Koshelev, G. Leaf, and V. Vinokur, Phys. Rev. B **61**, 1446 (2000).

[31] W. D. Gropp, H. G. Kaper, G. K. Leaf, D. M. Levine, M. Palumbo, and V. M. Vinokur, J. Comput. Phys. **123**, 254 (1996).

[32] T. Winiecki and C. Adams, Phys. Rev. B **65**, 104517 (2002).

[33] I. Sadovskyy, A. Koshelev, A. Glatz, V. Ortalan, M. Rupich, and M. Leroux, Phys. Rev. Appl. **5**, 014011 (2016).

[34] C. Reichhardt, A. van Otterlo, and G. T. Zimányi, Phys. Rev. Lett. **84**, 1994 (2000).

[35] C. Reichhardt, C. Olson, and F. Nori, Phys. Rev. B **61**, 3665 (2000).

[36] J. Groth, C. Reichhardt, C. Olson, S. B. Field, and F. Nori, Phys. Rev. Lett. **77**, 3625 (1996).

[37] V. Shklovskii, A. Soroka, and A. Soroka, J. Exp. Theor. Phys. **89**, 1138 (1999).

[38] Y. Mawatari, Phys. Rev. B **56**, 3433 (1997).

[39] Y. Mawatari, Phys. Rev. B **59**, 12033 (1999).

[40] H. Asai and S. Watanabe, Phys. Rev. B **77**, 224514 (2008).

[41] G. Crabtree, G. Leaf, H. Kaper, V. Vinokur, A. Koshelev, D. Braun, D. Levine, W. Kwok, and J. Fendrich, Physica C **263**, 401 (1996).

[42] A. Petković and T. Nattermann, Phys. Rev. Lett. **101**, 267005 (2008).
[43] T. Emig and T. Nattermann, Phys. Rev. Lett. **97**, 177002 (2006).
[44] A. Petković, T. Emig, and T. Nattermann, Phys. Rev. B **79**, 224512 (2009).
[45] M. C. Marchetti and V. M. Vinokur, Phys. Rev. Lett. **72**, 3409 (1994).
[46] M. C. Marchetti and V. M. Vinokur, Phys. Rev. B **51**, 16276 (1995).
[47] U. Dobramysl, H. Assi, M. Pleimling, and U. C. Täuber, Eur. Phys. J. B **86**, 228 (2013).
[48] H. Assi, H. Chaturvedi, U. Dobramysl, M. Pleimling, and U. C. Täuber, Phys. Rev. E **92**, 052124 (2015).
[49] H. Chaturvedi, H. Assi, U. Dobramysl, M. Pleimling, and U. C. Täuber, J. Stat. Mech. **2016**, 083301 (2016).
[50] H. Assi, H. Chaturvedi, U. Dobramysl, M. Pleimling, and U. C. Täuber, Molecular Simulation **42**, 1401 (2016).
[51] U. Dobramysl, M. Pleimling, and U. C. Täuber, Phys. Rev. E **90**, 062108 (2014).
[52] D. R. Nelson and V. M. Vinokur, Phys. Rev. B **48**, 13060 (1993).
[53] J. Das, T. J. Bullard, and U. C. Täuber, Physica A **318**, 48 (2003).
[54] T. J. Bullard, J. Das, G. L. Daquila, and U. C. Täuber, Eur. Phys. J. B **65**, 469 (2008).
[55] J. Bardeen and M. Stephen, Phys. Rev. **140**, A1197 (1965).
[56] M. Abdelhadi and K. A. Ziq, Supercond. Sci. Technol. **7**, 99 (1994).
[57] Video snapshots of the system in each of the six regimes (from multiple two-dimensional perspectives) can be viewed at `https://figshare.com/s/8a1e4bf34f463f988ebd`.